



Colorimetric plasmon resonance microfluidics on nanohole array sensors



Austin Hsiao^{a,d,1}, Manas Ranjan Gartia^{c,d,e,*,1}, Te-Wei Chang^{c,d}, Xinhao Wang^{c,d}, Pakapreud Khumwan^{b,d}, Gang Logan Liu^{a,c,d,*}

^a Department of Bioengineering, University of Illinois at Urbana-Champaign, Urbana, IL 61801, USA

^b Department of Bioengineering, University of Washington, Seattle, WA 98195, USA

^c Department of Electrical and Computer Engineering, University of Illinois at Urbana-Champaign, Urbana, IL 61801, USA

^d Micro and Nanotechnology Laboratory, University of Illinois at Urbana-Champaign, Urbana, IL 61801, USA

^e Department of Mechanical and Industrial Engineering, Louisiana State University, Baton Rouge, LA 70803, USA

ARTICLE INFO

Keywords:

Microfluidics
Surface plasmon
Colorimetric sensor
Nanohole array
Protein binding
Droplet formation

ABSTRACT

We present the label-free colorimetric visualization in microfluidics using plasmon resonance on a large-area and over a wide field-of-view ($>100\text{ mm}^2$) nanohole array device called nanoLycurgus Cup Array (nanoLCA). We demonstrate the spectral detection and colorimetric sensing of static solutions of different concentrations of glycerol–water confined in parallel microfluidic channels integrated with nanoLCA. Taking advantage of the large sensor area and the colorimetric sensing capability of nanoLCA, we visualize in real-time the modulation of two immiscible solutions (water and oil), generated with integrated flow-focus microfluidics, in a label-free manner. Finite Element Method (FEM) based simulation tool (COMSOL) was used to verify the droplet formation in the microfluidics. Finite Difference Time Domain (FDTD) electromagnetic simulation was used to identify the resonance modes of the plasmonic sensor. Finally, we demonstrate the real-time monitoring of streptavidin–biotin biomolecular interaction with the plasmonic biosensor.

© 2015 The Authors. Published by Elsevier B.V. This is an open access article under the CC BY-NC-ND license (<http://creativecommons.org/licenses/by-nc-nd/4.0/>).

1. Introduction

Traditional labels such as fluorophores, chromophores, or radioactive labels are widely used in microfluidic applications to visualize flow [1] or detect the presence or concentration of relevant species [2,3]. However, each of these labels has shortcomings including bleaching of fluorophores, non-specificity of chromophores, and steric blocking of conjugated labels [4–6]. In particular in microfluidics, labeling with multiple dyes may suffer from the low Reynolds number laminar flow and when introduced at high concentration, may alter the physical properties of the flow solution. Label-free detection based on optical techniques has revolutionized the ability to detect a broad range of biological samples such as protein–protein interaction, DNA hybridization simply based on the intrinsic dielectric permittivity of samples without the need for labeling [7–9]. In particular, label-free optical techniques such as surface plasmon resonance [10], photonic crystal

[11], and ring resonator [12] have been integrated with microfluidics to measure the changes in the refractive index near the surface of the sensor. However, these techniques require complex instrumentation for illumination and detection such as high-resolution spectrophotometer, high-intensity monochromatic light source, and prism coupling. In contrast, optical sensors consisted of nanohole array on a noble-metal film, which exhibit extraordinary optical transmission (EOT) [13], can be used with similar sensitivity to detect the changes in the refractive index near the surface of the sensor, with the advantage of simple collinear broadband illumination and portable spectrophotometer [14–16].

Previously, we have reported colorimetric surface plasmon resonance imaging using a nanohole array device called nanoLycurgus Cup Array (nanoLCA), in which we demonstrated high spectral sensitivity of the nanoLCA to the changes in the refractive index due to the presence of different refractive index solutions and to the surface binding of biological-relevant molecules such as protein–protein interaction and DNA hybridization [17]. Due to the unique transmission/reflection peak wavelengths of nanoLCA in the visible wavelength range, we were able to demonstrate visible colorimetric changes simply due to the changes in the refractive index on and near the surface of the sensor upon the changes of the presence or the concentration of the sample of interest. In

* Corresponding authors at: Department of Electrical and Computer Engineering, University of Illinois at Urbana-Champaign, Urbana, IL 61801, USA, and Department of Mechanical and Industrial Engineering, Louisiana State University, Baton Rouge, LA 70803, USA.

E-mail addresses: mgartia@lsu.edu (M.R. Gartia), loganliu@illinois.edu (G.L. Liu).

¹ Equal contribution.

this work, we extended the capability of nanoLCA to on-chip applications by integrating relevant microfluidic designs, such as parallel flow channels and droplet generator, and by demonstrating colorimetric visualization of static and transient dynamics of optically-transparent solutions, which previously could not be visualized in a colorimetric manner.

2. Materials and methods

2.1. Fabrication and microfluidic integration of nanohole sensor

The fabrication of the nanoLCA has been described in detail elsewhere [17] and in the Supporting Information. The nanoLCA has a periodicity of 350 nm and hole diameter of 100 nm, coated with 90 nm of Au and 9 nm of Ti for adhesion. The master mold with microfluidic design is designed using computer-aided design software and fabricated using stereolithography and the microfluidic design was replicated onto PDMS using traditional soft lithography method (Fig. 1A1). Since the PDMS-based microfluidic device comes into contact with the gold-coated surface of nanoLCA, the traditional bonding technique of oxygen plasma treatment is not sufficient to create a strong bond between the two substrates. The integration of the nanoLCA with the microfluidic device was accomplished using a “stamp and stick” method [6,18], which utilizes a UV-curable optical adhesive to act as an adhesive layer between the PDMS-based microfluidic device and the nanoLCA substrate (Fig. 1A2–A4). A thin layer of UV-curable optical adhesive (Norland 61, Norland Products, NJ, USA) is formed on a flat substrate by spin-coating at 6000 rpm for 120 s. The PDMS mold with microfluidic design is brought into contact with the thin

layer of UV-curable polymer adhesive for 30 s. Then the PDMS substrate with microfluidic design is removed and subsequently brought into contact with the nanoLCA substrate. The bonded PDMS–nanoLCA substrate is exposed to UV lamp for five minutes and then placed on a hot plate set at 65 °C for 12 h for adhesive aging. The bonding between the nanoLCA substrate and the microfluidic PDMS substrate has withstood flow rates up to 30 $\mu\text{L min}^{-1}$ without any leaks or delamination and is compatible with different solvent types including mineral oil and deionized water. The UV-curable adhesive based bonding is a facile process in terms of required equipment and processing time relative to oxygen plasma treatment. A schematic of the experimental set-up is shown in Fig. 1B. The colorimetric imaging was performed in transmission and reflection modes with using illumination provided by a halogen lamp and imaging using a 5 \times objective and a CCD camera.

Static spectral and optical colorimetric characterization of microfluidic nanoLCA was performed using a parallel-channel microfluidic device bonded to the nanoLCA substrate (Fig. 1C). The parallel-channel design (width: 500 μm , height: 200 μm) allows for maximal area usage of the nanoLCA substrate (Fig. 1D–G) by accommodating multiple solutions on a single device, with minimal volume of sample needed (~ 100 nL).

2.2. Integration of droplet generator

After curing, the PDMS substrate was excised and the bonding surface was cleaned and protected using an adhesive tape. The fluid connection ports were created using an 18-gauge blunt-end needle. UV curable polymer-based “stamp and stick” method was

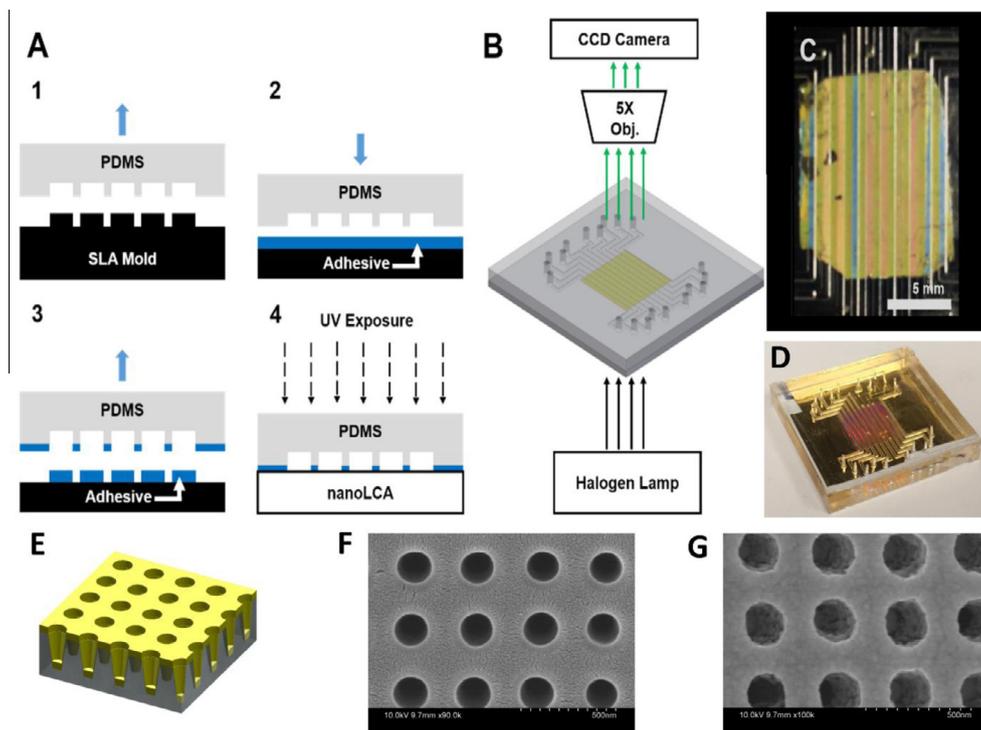


Fig. 1. Schematic of the construction and the assembly of microfluidic nanoLCA sensor. (A1) Polydimethylsiloxane (PDMS)-based microfluidic device is replicated from a stereolithography (SLA) master mold. (A2 and A3) The microfluidic device is brought into contact with a thin layer of UV-curable optical adhesive and the adhesive is transferred onto the contacted PDMS surface. (A4) The adhesive-coated microfluidic device is brought into contact with the nanoLCA and the adhesive was cured by exposure to UV light. (B) Colorimetric imaging was performed in transmission and reflection modes with using illumination provided by a halogen lamp and imaging using a 5 \times objective and a CCD camera. (C) A microfluidic device with ten parallel channels bonded to the nanoLCA layer, perfused with various aqueous solutions (yellow and red color appearances) and empty (blue color appearance) (channel width: 500 μm). (D) An optical image of the microfluidic integrated nanoLCA sensor. (E) Schematics of the nanoLCA sensor in 3D-perspective. (F and G) SEM images with normal and angled view. (For interpretation of the references to colour in this figure legend, the reader is referred to the web version of this article.)

used to bond the PDMS device to the nanoLCA. Prior to the adhesion step, the contact surface of the nanohole array substrate was rinsed with isopropanol and deionized water twice and then dried with Nitrogen gun. In addition, the PDMS substrate and the rinsed nanohole array substrate were further cleaned with oxygen plasma for 1 min. Two syringe pumps (Harvard Apparatus, MA, USA) were used to perfuse the two solutions (oil and water) into the microfluidic device at a rate of $10 \mu\text{L min}^{-1}$ (water) and $5 \mu\text{L min}^{-1}$ (oil). At steady state, water-in-oil droplets were generated at a rate of approximately 1 Hz.

2.3. Immobilization of biotinylated thiol

For streptavidin–biotin experiments, 33 mM of biotinylated thiol (Nanoscience, Phoenix, AZ) solution in anhydrous ethanol was flowed into the microfluidic nanohole array sensor overnight to form a self-assembled monolayer. After the incubation, the microfluidic channel was rinsed with ethanol and water twice, and after rinsing, a control spectrum was measured using phosphate buffered solution as a blank. Streptavidin solution was flowed in the microfluidic channel as the time-trace measurement commenced.

3. Results and discussion

3.1. Electromagnetics numerical simulation

In order to understand the plasmonic resonance property of the nanoLCA biosensor 3D-FDTD electromagnetic simulation has been performed by using FDTD software package from Lumerical Solutions. The total simulation region was set to $350 \text{ nm} \times 350 \text{ nm} \times 800 \text{ nm}$. The modeling of nanostructure was based on the observation of SEM images of nanoLCA device. The periodicity of the nanohole array was 350 nm. The diameter of nanohole at the top surface and the depth of the hole were taken as 200 and 500 nm respectively. The sidewall slew rate was 85° . The cross-section of simulation model is schematically shown in the [Supplementary Information](#). The boundary conditions in x and y directions were set to be periodic to present the array effect of nanoLCA device. The perfect matching layer (PML) was applied in z -directional boundary condition to minimize the simulation error from boundary reflection. The x -axis polarized plane wave was set to propagate normal to the substrate ($-z$ direction). The mesh size was set to be 1.5 nm in order to minimizing the stair-case and dispersion error. The simulation results is shown in [Fig. 2](#). [Fig. 2A](#) and [B](#) depicts the simulated and experimental transmission spectra of nanoLCA sensor immersed with three different dielectric materials (air, water and oil) and the cross-sectional electric and magnetic fields of cup-shaped nanostructure at resonance peaks. Overall the simulated result predicts very well with experimental data. The major difference is the absence of first resonance peak with water and oil (461 nm in water and 479 nm in oil) in the experimental spectra. The x -directional electric field (E_x) at those wavelengths in [Fig. 2C](#) shows clearly these two resonance peaks come from Fabry–Perot modes inside nanocavity. The possible reason why it does not show in experiment is the presence of sidewall nanoparticles, which significant alter the boundary conditions and destroy the formation of Fabry–Perot confined mode. Another minor difference is the peak shift of the second resonance peaks with water and oil when comparing simulated ($\lambda = 506 \text{ nm}$ in water and 520 nm in oil) and experimental ($\lambda = 513 \text{ nm}$ in water and 539 nm in oil) data. From the absolute value of E_x in [Fig. 2C](#) the enhanced field is confined inside the rim of Au nanohole. As a result, the origin of these two modes can be attributed to localized surface plasmon resonance

(LSPR). The variation of resonance peak position in experiment compared to the simulation is reasonable due to the fabrication variance between the simulation model and actual device. The two modes with air ($\lambda = 496$ and 541 nm) as superstrate are merged into one resonance peak in experiment ($\lambda = 527 \text{ nm}$). The peak at $\lambda = 496 \text{ nm}$ can also be attributed to LSPR modes from the absolute value of E_x in [Fig. 2C](#). Nevertheless, the peak at $\lambda = 541 \text{ nm}$ as well as the third peak in water and oil cases ($\lambda = 612 \text{ nm}$ in water and 641 nm in oil) is related to surface-plasmon-resonance-Bloch-wave (SPP-BW) by the observation of z -directional electric field (E_z) and y -directional magnetic distribution (H_y). A theoretical approximation of the peak wavelength in a nanohole array due to surface-plasmon-polariton-Bloch-wave ($\lambda_{\text{SPP-BW}}$) is given as $\lambda_{\text{SPP-BW}} = \frac{p}{\sqrt{i^2 + j^2}} \sqrt{\frac{\epsilon_m \epsilon_d}{\epsilon_m + \epsilon_d}}$, where p is periodicity of the nanohole array, i and j are the scattering orders, ϵ_m and ϵ_d are the dielectric constants of the metal and the dielectric solution respectively [19]. Similar peaks have been observed in nanohole array devices with comparable array dimensions [20,21] and the peaks were assigned to the two resonance modes $\lambda_{(1,0)}$ of the surface plasmon-polariton-Bloch wave generated in the nanohole array from the metal-solution interface.

3.2. Optical characterization

To characterize the spectral sensitivity of nanoLCA, different concentrations of glycerol diluted in deionized water (water only, 1%, 5%, 10%, 20%, 30%, 40%, 50% v/v) were prepared to generate solutions with different refractive index and each solution was perfused into a different parallel channel on top of the nanoLCA. Transmission spectrum of each concentration solution confined in a channel was measured using a multispectral optical imaging system [22], which utilizes a wavelength-controllable monochromatic light source ($\lambda = 400\text{--}800 \text{ nm}$, $\Delta\lambda = 1 \text{ nm}$) and a monochromatic camera synchronized with the light source. With increasing refractive index (i.e. increasing glycerol concentration), the second peak wavelength around 600 nm red shifts, that is, it shifts to longer wavelengths ([Fig. 3A](#)). That red shift is expected from the above surface-plasmon-polariton-Bloch-wave ($\lambda_{\text{SPP-BW}}$) equation, which indicates the increase of dielectric constant of the dielectric material will give rise to an increase in the wavelength of SPP-Bloch wave. The sensitivity was calculated by measuring the change in the wavelength of the second intensity peak ($\Delta\lambda$) as the refractive index of the glycerol solution was changed (Δn) ([Fig. 3B](#)). The measured sensitivity (S), which was calculated as $(\frac{\Delta\lambda}{\Delta n})$, was 247 nm RIU^{-1} ($R^2 = 0.99$) in the range of refractive index from 1.33 to 1.4137, comparable to other sensors (ring resonator $S \sim 246 \text{ nm-RIU}^{-1}$ [12], nanohole array $S \sim 333\text{--}470 \text{ nm-RIU}^{-1}$ [14,16,23]). The figure of merit (FOM), a metric for comparing sensing performance of plasmonic sensors, is calculated as $(\frac{\Delta\lambda}{\Delta n}) (\frac{1}{\Delta w})$, where Δw is the full-width-half-maximum (FWHM) of the resonance peak. The FOM for the gold-coated nanoLCA used in the experiment is 3.3 with a FWHM of 75 nm.

3.3. Colorimetric plasmonic imaging

Due to the fact that the change in the transmission peak wavelengths of nanoLCA, in response to the change of refractive index, is in the visible wavelength range ($\lambda = 400\text{--}800 \text{ nm}$), there is a corresponding change in the color appearance of the transmitted light. This phenomenon was utilized previously by capturing color images and correlating the intensity change of RGB channels of the images with the change in refractive index [17]. In this work, we utilized simple collinear illumination in transmission and reflection modes to colorimetrically detect the change in refractive

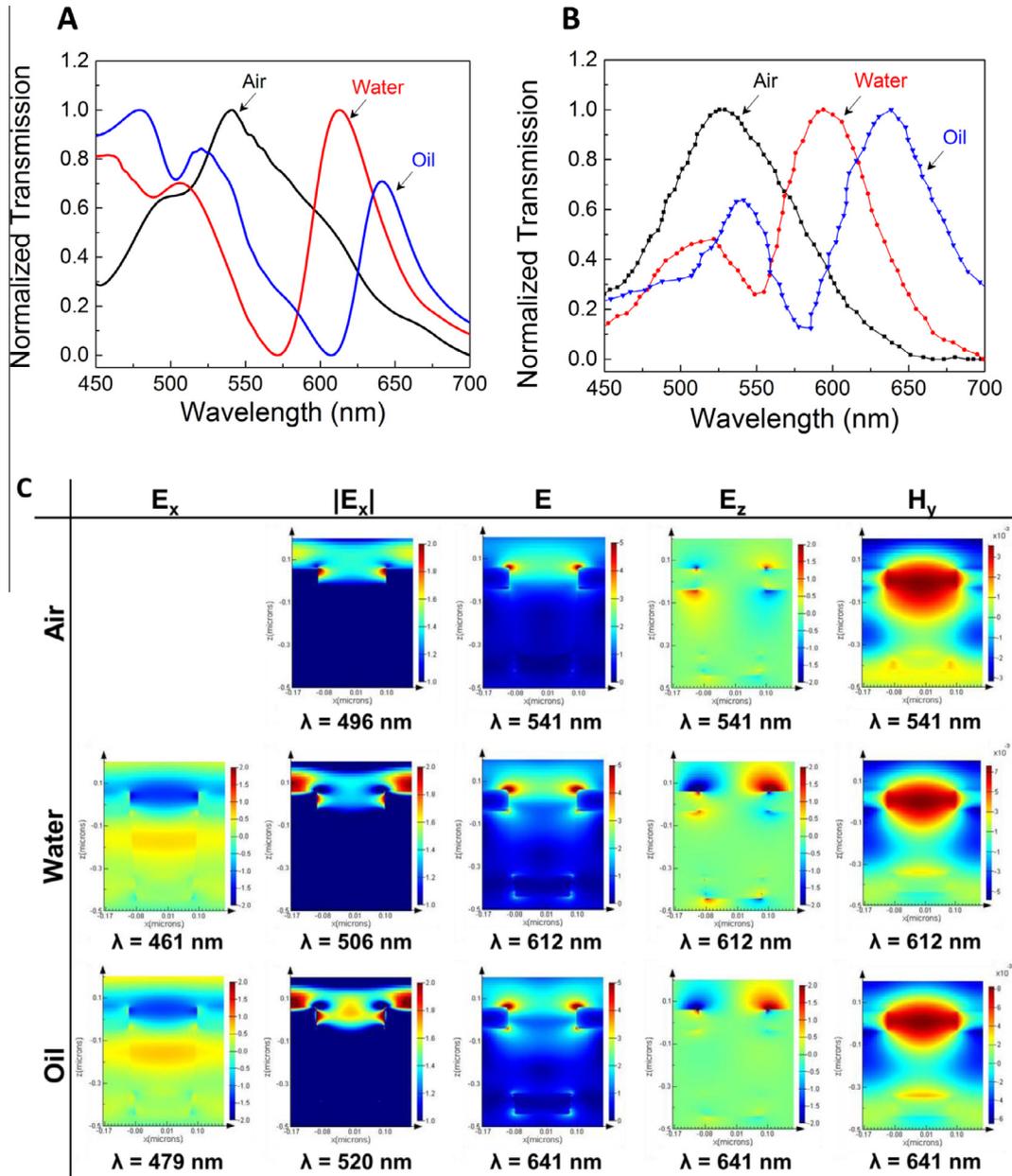


Fig. 2. The (A) simulated and (B) experimental transmission spectra of nanoLCA device immersed in three different dielectric materials, air, water and oil; (C) Cross-sectional electric and magnetic near field distribution at resonance peaks of three cases mentioned above.

index. Each of the microfluidic nanoLCA channels filled with glycerol solution was illuminated by a halogen lamp collimated with a condenser lens and imaged using a $5\times$ objective lens coupled to a color CCD camera (Olympus, PA, USA). Fig. 3C and E shows cropped region from the obtained optical image of the microfluidic nanoLCA channel for each concentration of glycerol solution, from transmission and reflection modes respectively. In transmission mode, the color appearance changes from green to red as the refractive index increases (i.e. glycerol concentration increases), which agrees with the spectral measurement. For each image (i.e. one concentration/one refractive index), we extracted red, green, and blue (RGB) channels and for each color channel, we computed the average of the normalized intensity (normalized by total intensity, e.g. for red channel, $R_{\text{norm}} = \frac{R_{\text{raw}}}{R_{\text{raw}} + G_{\text{raw}} + B_{\text{raw}}}$) of four separate regions from the image. Fig. 3D shows the normalized intensity of red and green channels extracted from optical transmission images versus the change in refractive index. Consistent with the

red shift from the spectral measurements, the normalized intensity of red channel increased and the normalized intensity of green channel decreased with increasing refractive index. The colorimetric sensitivity of R and G channels are 1.18 RIU^{-1} and -1.11 RIU^{-1} , respectively. That is, for a change of 0.01 refractive index unit, there is approximately 1% increase and decrease of normalized intensity of R and G channels. This is slightly lower than the bulk sensitivity characterized in a similar nanohole array device (periodicity: 420 nm, diameter: 225 nm) [21]; however, this may be due to differences in the optical detection setup and the larger periodicity of the array, which increases the bulk sensitivity [20,24]. In the reflection mode (Fig. 3F), we observed the colorimetric response to change in refractive index in a reciprocal manner to that of the transmission mode, that is the minimum intensity wavelength in transmission coincides with the maximum intensity wavelength in reflection mode [25]. With increasing refractive index, in reflection mode, there was a decrease in the

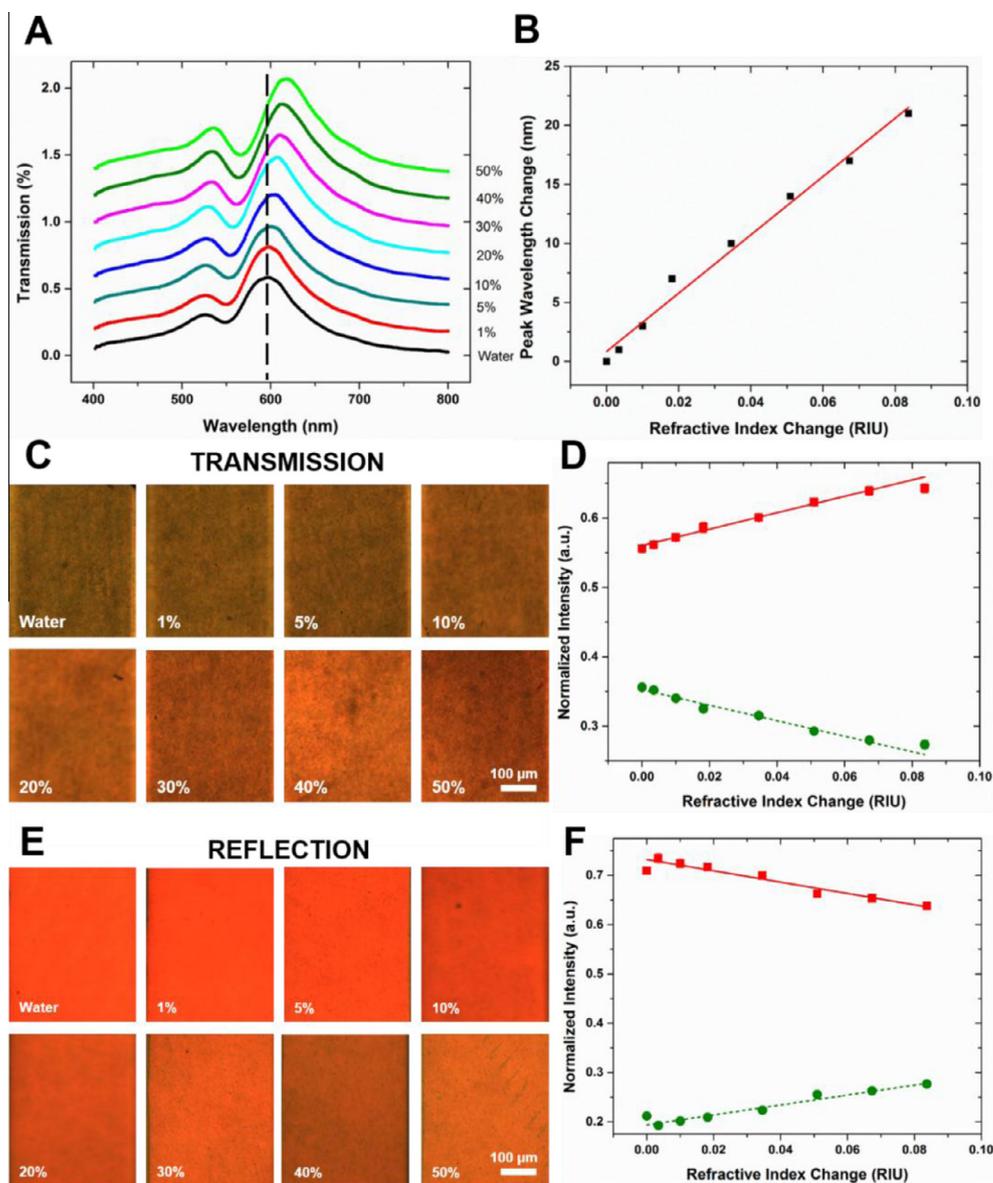


Fig. 3. Spectral and colorimetric characterizations of nanoLCA in the response to changes in refractive index due to the presence of increasing concentration of glycerol solutions. (A) Transmission spectra of nanoLCA with increasing concentrations of glycerol solutions (dashed line was added to aid the visualization of peak wavelength shift). (B) Refractive index sensitivity of nanoLCA characterized by linearly fitting the change in peak wavelength versus the change in refractive index. The sensitivity was calculated to be 247 nm RIU^{-1} ($R^2 = 0.99$) in the range of $\text{RI} = 1.33\text{--}1.4137$. (C) Optical transmission images of different channels of microfluidic nanoLCA filled with increasing concentrations of glycerol solution. (D) In transmission imaging, the normalized intensity of red channel (red solid line) is observed to increase linearly and the normalized intensity of green channel (green dashed line) is decreasing linearly with increasing refractive index change. (E) Optical reflection images of different channels of microfluidic nanoLCA (same location as the transmission images) filled with increasing concentrations of glycerol solution. (F) In reflection imaging mode, a reciprocal normalized intensity response to increasing was observed for red and green channels compared those in the transmission mode. That is, with increasing refractive index change, the normalized intensity of red channel (red solid line) is observed to decrease linearly and the normalized intensity of green channel (green dashed line) is increasing linearly. (For interpretation of the references to colour in this figure legend, the reader is referred to the web version of this article.)

normalized intensity of R channel and an increase in the normalized intensity of G channel. The calculated colorimetric sensitivity in reflection mode was -1.15 RIU^{-1} and 1.01 RIU^{-1} for R and G channels respectively.

Optical colorimetric sensing of different refractive index solutions on nanoLCA was possible due to the fact that the change in peak wavelength is within the visible wavelength range, specifically in the green–red range. Other nanohole array devices have been reported with similar optical changes in the visible and near-infrared wavelength range [26–28]. However, due to limitations such as peak wavelength shift in near-infrared wavelength range, small sensor area ($15 \mu\text{m}$ by $15 \mu\text{m}$ only), or single

wavelength light source (intensity variations only), spectral/colorimetric changes due to changes in refractive index and spatial localization of the spectral changes cannot be simultaneously visualized using existing optical microscopy systems and instead requires custom illumination set up and high magnification objective (e.g. $100\times$). In contrast, nanoLCA devices have been fabricated with a minimum sensor area of $1 \text{ cm} \times 1 \text{ cm}$, which contains up to 2.8 million individual nanocups with a periodicity of 350 nm . The large sensor area combined with sensitive colorimetric sensing in the visible wavelength range enables real-time colorimetric sensing over wide field-of-view with spatial localization of micro–macro fluidic dynamic on top of the nanoLCA.

3.4. Plasmonic imaging of droplet formation

To demonstrate real-time colorimetric sensing and spatial localization of different refractive indices with nanoLCA, we chose two solutions (water and mineral oil) due to the large difference in refractive index ($n = 1.332$ and $n = 1.467$) and the immiscibility between the two solutions. These solutions are widely used in droplet formation with water in dispersed phase and oil in continuous phase [29,30]. Optical images of the two solutions on nanoLCA showed the expected red shift appearance in the transmission mode and the blue shift appearance in the reflection mode due to the increase in refractive index (Fig. 4A). The red shift in transmission mode is confirmed with the measured transmission spectra of the two solutions, where the transmission spectrum of water has an intensity peak at 589 nm and that of oil has an intensity peak at 635 nm. To spatially modulate the two immiscible solutions, we fabricated a microfluidic device with flow focusing geometry to generate water droplets in oil emulsion (Fig. 4B) with the flow focus junction placed on the nanoLCA. Fig. 4C shows the close up view of the water inlet channel and the two oil inlet channels at the flow focusing junction on nanoLCA. Note that in this reflection image the contrast in the color appearance of the two immiscible solutions is apparent and the interface between the two appears as dark regions. The two solutions were perfused into the microfluidic device using two syringe pumps (Harvard Apparatus, MA, USA) at a rate of $10 \mu\text{L min}^{-1}$ (water) and $5 \mu\text{L min}^{-1}$ (oil), and at steady state, water-in-oil droplets were generated at a rate of

approximately 1 Hz. Fig. 4D shows a series of time lapsed images of generated water-in-oil droplets traversing across a selected region on nanoLCA (see the recorded movie in Supporting Information). Due to the large sensor area, the entirety of the generated droplet can be visualized at relatively high temporal resolution. More importantly, the difference in refractive index of the water droplet in oil emulsion can be visualized in real-time as the water droplets wetted the surface of nanoLCA as they traveled toward the outlet. Upon closer inspection, we observed partial wetting at the leading edge of the water droplet where there were green streaks trailing the droplet edge, indicating the gradual displacement of oil molecules by the water molecules as the droplet wets the surface. Likewise, the observed green streak inside the droplet away from the edge of the droplet was due to a thin layer of oil that was trapped on the surface of nanoLCA. This demonstrates the high sensitivity to the refractive index of the solution immediately adjacent to the surface where the evanescent field penetrates approximately 200–300 nm into the dielectric medium [31].

3.5. Finite element modeling of droplet formation

In order to elucidate the droplet formations in microfluidics, we simulated the geometry and flow conditions using COMSOL. The laminar two-phase flow model with level set interface was used to simulate this periodic droplet formation. The flow is assumed to be incompressible and laminar; that is, the Reynolds number is low to moderate. The Navier–Stokes equation was solved in

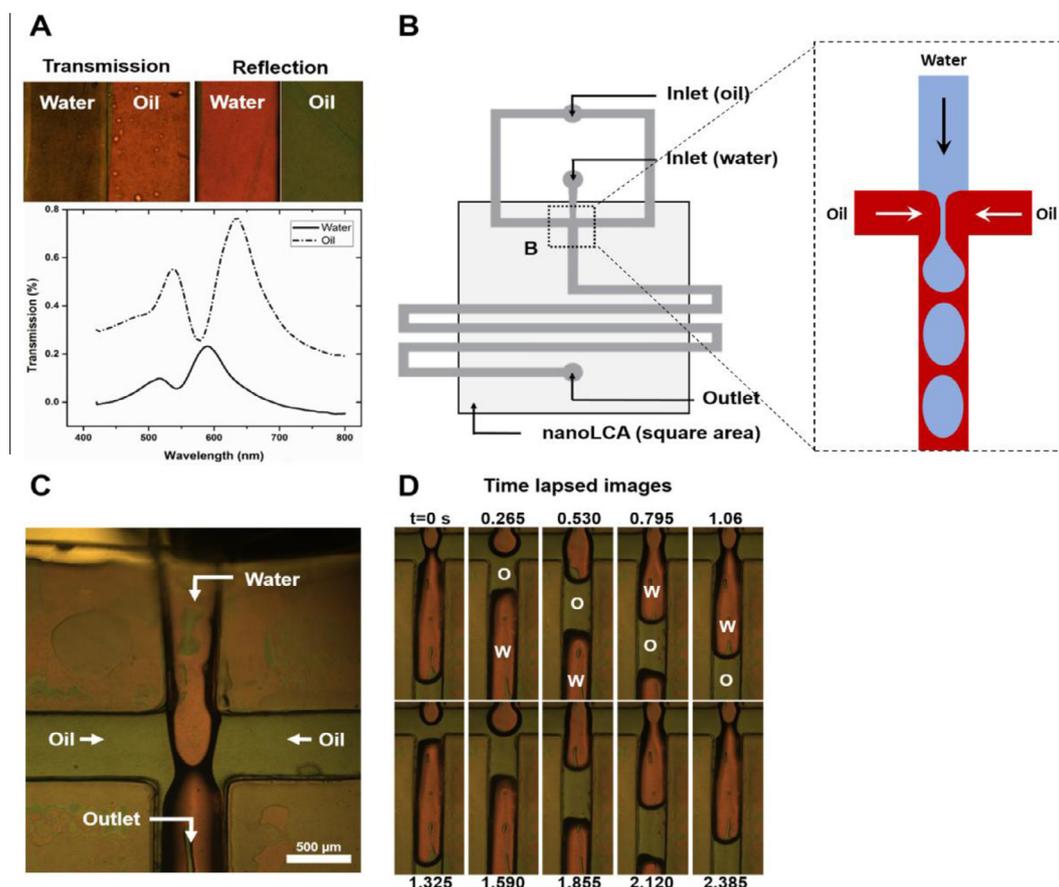


Fig. 4. Modulation of two immiscible solutions (water and oil) with different refractive indices on microfluidic nanoLCA via micro-droplet generation. (A) Top row shows the transmission (left) and reflection (right) colorimetric images of water and oil on the nanoLCA. Bottom plot is the transmission spectra of water and oil on nanoLCA. (B) Microfluidic scheme for droplet generation, using water-in-oil emulsion, placed over the nanoLCA. Close-up view of the microfluidic droplet generation nozzle region (dotted area from figure B) with top inlet for water and side inlets for oil (solid arrow indicates the direction of the flow) is schematically shown at the right. (C) Reflection image of droplet generation on nanoLCA (corresponding actual image of device shown schematically in B). (D) Time lapsed reflection images of water (W) droplet formation, release, and re-formation in oil (O) emulsion at the nozzle region.

considering the level-set function (low reinitialization parameter for immiscible fluid). Time dependent analysis was performed to detect the volume fraction of water at certain position. The ratio of flow rate for water and oil is 2, which is consistent with experiment.

3.6. Image analysis

The colorimetric sensing of the modulation of refractive indices was quantified for green and red channels in both transmission and reflection mode measurements (Fig. 5). In transmission mode, the red shift of the peak wavelength with the increase in the value of refractive index (from water to oil) can be observed as an increase in the intensity of the red channel and a decrease in the intensity of the green channel (Fig. 5A and B). Conversely, in reflection mode, the intensity of red channel decreases with an increase in refractive index (from water to oil), and the intensity of green channel increases accordingly (Fig. 5C and D). The difference in the colorimetric sensitivity between the transmission mode and reflection mode may be due to the stronger SPP coupling on the metal-solution side when illuminated from the solution side (reflection mode); similar observations have been when the two modes were compared in nanohole arrays [25,32]. This modulation of two immiscible solutions can be colorimetrically distinguished and spatially localized with in the field of view of the objective lens; specifically the outline of the droplet and the surface wetting of the droplet are visible. The colorimetric sensing capability of

microfluidic nanoLCA over long term time traces of modulation showed consistent and robust results. The COMSOL simulation verified this periodic phenomenon by detecting the volume fraction of water at a certain position (1250 μm away from the inlet of water). Because of the refractive index difference between these two immiscible liquids, they can be distinguished periodically from the change in color.

3.7. Kinetics of biomolecular binding on plasmonic nanohole sensor

In order to demonstrate the kinetic measurement of biomolecule interaction on the surface of nanohole array, we used streptavidin–biotin binding as a model system. Streptavidin–biotin has one of the highest known affinity ($K_a \sim 10^{15} \text{ M}^{-1}$), which has been exploited to functionalize biomolecules such as proteins, nucleic acids, antibodies, and synthetic particles such as magnetic beads [33,34]. For the kinetic measurements, we utilized a 200 nm fluorescently labeled microsphere (Bangs Laboratories, Fishers, IN) coated with streptavidin, which allowed us to confirm the presence of the streptavidin with fluorescence imaging. To functionalize the surface of the nanohole array sensor, we immobilized biotinylated thiol, which formed a self-assembled monolayer with the biotin moiety directed away from the surface. The streptavidin solution was flowed into the microfluidic channel using a syringe pump with controllable flow rate and the time trace measurement of the light spectrum was continually recorded for a period of up to 1 h. Fig. 6 show the typical sensorgram with the association and

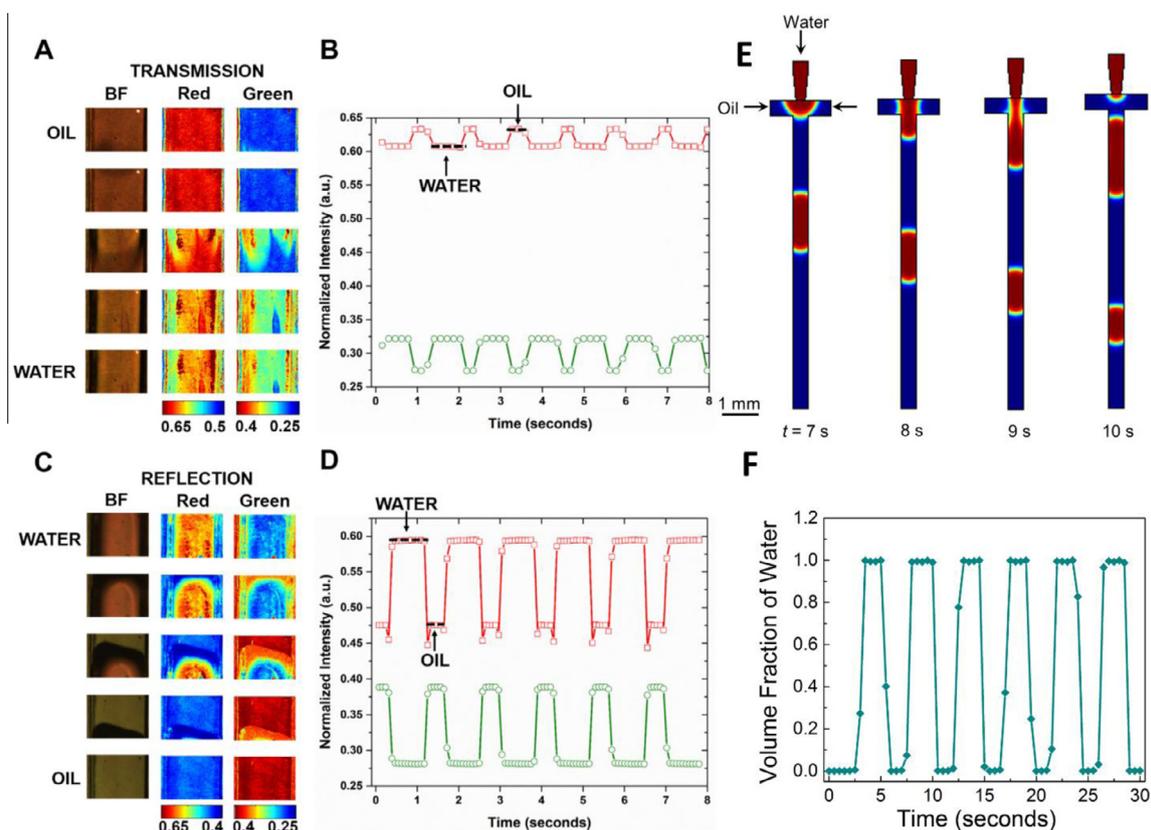


Fig. 5. Colorimetric sensing of two immiscible solutions (water and oil) with different refractive indices on nanoLCA modulated by microfluidic droplet generation scheme. (A) Colorimetric sensing based on optical (BF) transmission images of two immiscible solutions modulated over a region of nanoLCA. Flow over of oil (higher refractive index fluid) on nanoLCA resulted in an increase of normalized intensity of red channel and a decrease in the normalized intensity of green channel. (B) Long term modulation of droplets of water and oil on nanoLCA resulted in consistent corresponding modulation of normalized intensity of red and green channels. (C) In reflection mode, flow over of oil (higher refractive index fluid) on nanoLCA resulted in a decrease of normalized intensity of red channel and an increase in the normalized intensity of green channel. (D) In reflection mode, higher normalized intensity contrast for both red and green channels can be observed, compared to those in transmission mode, in response to the modulation of water and oil on nanoLCA. (E) COMSOL simulation for the periodic droplet formation of two immiscible laminar flow. Volume fraction of water is displayed here changing with time from 7 s to 10 s. (F) The volume fraction of water at certain position changes periodically with time within 30 s. (For interpretation of the references to colour in this figure legend, the reader is referred to the web version of this article.)

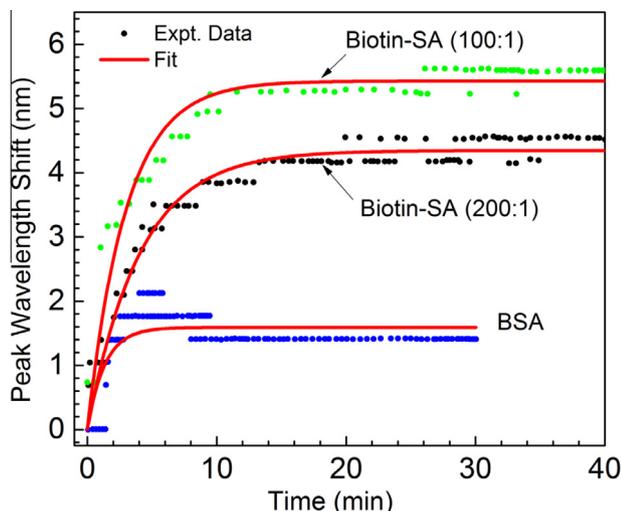


Fig. 6. Streptavidin (SA)-biotin representative association curve on nanohole array sensor immobilized with biotinylated thiol. Two concentrations (100:1 and 200:1 dilution ratio) of streptavidin solution was used. The flow rate used was 20 $\mu\text{L}/\text{min}$. Bovine serum albumin (BSA) association curve on Au nanohole array sensor via adsorption. 1 mg/mL BSA solution was injected at 40 $\mu\text{L}/\text{min}$ into the microfluidic channel around the 2-min mark.

the dissociation stages of the binding event between the streptavidin-coated microspheres and the biotin moiety on the surface. The association stage shows the rapid accumulation of the streptavidin-coated microspheres on the surface, which increases the local refractive index near the surface. Subsequently, the peak wavelength was observed to red shift that is to shift to higher wavelength, as the local refractive index increases. The biomolecular interactions between immobilized protein biotin and target protein streptavidin (SA) can be modeled with the following equation:

$$d[\text{SA-Biotin}]/dt = k_a[\text{SA}][\text{Biotin}] - k_d[\text{SA-Biotin}] \quad (1)$$

The rate of change of peak wavelength shift, $d\Delta\lambda/dt$ is related to the formation of protein complex [SA-Biotin]. The exponential binding curve $\Delta\lambda(t)$ can be obtained by integrating Eq. (1) with the boundary condition $\Delta\lambda(0) = 0$, yielding

$$\Delta\lambda(t) = \Delta\lambda_0[1 - e^{-(k_a[\text{SA}] + k_d)t}] \quad (2)$$

where $\Delta\lambda_0 = (k_a[\text{SA}]\Delta\lambda_{\text{max}})/(k_a[\text{SA}] + k_d)$.

The experimental data were fit using Eq. (2) resulting in $\Delta\lambda = 5.428(1 - e^{-0.33315t})$ for 100:1 dilution, where t is in min.

$\Delta\lambda = 4.345(1 - e^{-0.24612t})$ for 200:1 dilution, and $\Delta\lambda = 1.591(1 - e^{-0.74319t})$ for BSA. The rate constants are found to be order of magnitude higher than similar binding reported using EOT devices [33] suggesting higher surface coverage on the present biosensor (nanoLCA devices).

Further, we quantitatively extract the effective streptavidin layer thickness, d_p using the expression $\Delta\lambda = m\Delta n(1 - e^{-2d_p/L_d})$, where m = bulk sensitivity of the device, Δn is the change in refractive indices between protein and buffer, and L_d is the decay length of surface plasmon of the biosensor into the solution, which is measured to be 132 nm for the present work. If we consider the refractive index of protein to be 1.5, the effective protein thickness is calculated to be 3.0 nm, which agrees well with the SA monolayer thickness reported in the literature [35–37].

4. Conclusion

The implication of this colorimetric visualization of aqueous-based and non-aqueous-based solutions is direct

observation of fluid phenomena such as laminar or turbulent flow and mixing without the need for the addition of contrast agent. In addition, due to the high colorimetric sensitivity to the refractive index of the nanoLCA, the use of a spectrometer or other complex instrumentation is not required to detect the optical changes within the fluid flow. Applications such as droplet generation for discretize reaction or droplet-based detection, microfluidic nanoLCA can be used to monitor the kinetics of the ongoing reaction within the droplet. Given the ease of fabrication and integration of nanoLCA with microfluidics, the device the promising as a portable colorimetric on-chip biosensors platform.

Conflict of interest

The authors declare that there are no conflicts of interest.

Appendix A. Supplementary data

Supplementary data associated with this article can be found, in the online version, at <http://dx.doi.org/10.1016/j.sbsr.2015.06.001>.

References

- [1] D. Sinton, *Microfluid Nanofluid* 1 (2004) 2–21.
- [2] A.H.C. Ng, U. Uddayasankar, A.R. Wheeler, *Anal. Bioanal. Chem.* 397 (2010) 991–1007.
- [3] A. Bange, H.B. Halsall, W.R. Heineman, *Biosens. Bioelectron.* 20 (2005) 2488–2503.
- [4] J.R. Lakowicz, *Principles of Fluorescence Spectroscopy*, Springer, New York, 2006.
- [5] J.W. Lichtman, J.A. Conchello, *Nat. Methods* 2 (2005) 910–919.
- [6] J. Tate, G. Ward, *The Clinical biochemist reviews, Aus. Assoc. Clin. Biochem.* 25 (2004) 105–120.
- [7] X. Fan, I.M. White, S.I. Shopova, H. Zhu, J.D. Suter, Y. Sun, *Anal. Chim. Acta* 620 (2008) 8–26.
- [8] A.J. Haes, R.P. Van Duyne, *Anal. Bioanal. Chem.* 379 (2004) 920–930.
- [9] M.A. Cooper, *Anal. Bioanal. Chem.* 377 (2003) 834–842.
- [10] V. Kodoyianni, *Biotechniques* 50 (2011) 32–40.
- [11] C.J. Choi, I.D. Block, B. Bole, D. Dralle, B.T. Cunningham, *IEEE Sens. J.* 9 (2009) 1697–1704.
- [12] C.F. Carlborg, K.B. Gylfason, A. Kazmierczak, F. Dortu, M.J. Banuls Polo, A. Maquieira Catala, G.M. Kresbach, H. Sohlstrom, T. Moh, L. Vivien, J. Popplewell, G. Ronan, C.A. Barrios, G. Stemme, W. van der Wijngaart, *Lab Chip* 10 (2010) 281–290.
- [13] T.W. Ebbesen, H.J. Lezec, H.F. Ghaemi, T. Thio, P.A. Wolff, *Nature* 391 (1998) 667–669.
- [14] R. Gordon, D. Sinton, K.L. Kavanagh, A.G. Brolo, *Acc. Chem. Res.* 41 (2008) 1049–1057.
- [15] A. De Leebeek, L.K.S. Kumar, V. de Lange, D. Sinton, R. Gordon, A.G. Brolo, *Anal. Chem.* 79 (2007) 4094–4100.
- [16] A.G. Brolo, R. Gordon, B. Leatham, K.L. Kavanagh, *Langmuir* 20 (2004) 4813–4815.
- [17] M.R. Gartia, A. Hsiao, A. Pokhriyal, S. Seo, G. Kulsharova, B.T. Cunningham, T.C. Bond, G.L. Liu, *Adv. Opt. Mater.* 1 (2013) 68–76.
- [18] S. Satyanarayana, R.N. Karnik, A. Majumdar, *J. Microelectromech. Syst.* 14 (2005) 392–399.
- [19] C. Genet, T.W. Ebbesen, *Nature* 445 (2007) 39–46.
- [20] M. Najiminaini, F. Vasefi, B. Kaminska, J.J.L. Carson, *Appl. Phys. Lett.* 100 (2012) 063110.
- [21] C. Escobedo, S. Vincent, A.I.K. Choudhury, J. Campbell, A.G. Brolo, D. Sinton, R. Gordon, *J. Microchem. Microeng.* 21 (2011) 115001.
- [22] G.L. Liu, J.C. Doll, L.P. Lee, *Opt. Exp.* 13 (2005) 8520–8525.
- [23] S.H. Lee, N.C. Lindquist, N.J. Wittenberg, L.R. Jordan, S. Oh, *Lab Chip* 12 (2012) 3882–3890.
- [24] J.P. Monteiro, L.B. Carneiro, M.M. Rahman, A.G. Brolo, M.J.L. Santos, J. Ferreira, E.M. Giroto, *Sensor Actuat B Chem.* 178 (2013) 366–370.
- [25] W.L. Barnes, W.A. Murray, J. Dintinger, E. Devaux, T.W. Ebbesen, *Phys. Rev. Lett.* 92 (2004) 107401.
- [26] C. Escobedo, Y. Chou, M. Rahman, X. Duan, R. Gordon, D. Sinton, A.G. Brolo, J. Ferreira, *Analyst* 138 (2013) 1450–1458.
- [27] M. Najiminaini, F. Vasefi, B. Kaminska, J.J.L. Carson, *Sci. Rep.* 3 (2013) 2589.
- [28] A.A. Yanik, A.E. Cetin, M. Huang, A. Artar, S.H. Mousavi, A. Khanikaev, J.H. Connor, G. Shvets, H. Altug, *Proc. Natl. Acad. Sci. USA* 108 (2011) 11784–11789.
- [29] C. Chang, J. Sustarich, R. Bharadwaj, A. Chandrasekaran, P.D. Adams, A.K. Singh, *Lab Chip* 13 (2013) 1817–1822.
- [30] A. Chen, T. Byvank, W. Chang, A. Bharde, G. Vieira, B.L. Miller, J.J. Chalmers, R. Bashir, R. Sooryakumar, *Lab Chip* 13 (2013) 1172–1181.

- [31] L.S. Jung, C.T. Campbell, T.M. Chinowsky, M.N. Mar, S.S. Yee, *Langmuir* 14 (1998) 5636–5648.
- [32] L. Wu, P. Bai, X. Zhou, E.P. Li, *IEEE Photon. J.* 4 (2012) 26–33.
- [33] A.F. Coskun, A.E. Cetin, B.C. Galarreta, D.A. Alvarez, H. Altug, A. Ozcan, *Sci. Rep.* 4 (2014) 6789.
- [34] S. Wu, K. Lee, A. Chiou, X. Cheng, P. Wei, *Small* 9 (2013) 3532–3540.
- [35] Y. Gao, Q. Gan, Z. Xin, X. Cheng, F.J. Bartoli, *ACS Nano* 5 (2011) 9836–9844.
- [36] M.E. Stewart, N.H. Mack, V. Malyarchuk, J.A.N.T. Soares, T. Lee, S.K. Gray, R.G. Nuzzo, J.A. Rogers, *Proc. Natl. Acad. Sci. USA* 103 (2006) 17143–17148.
- [37] L. Haussling, H. Ringsdorf, F.J. Schmitt, W. Knoll, *Langmuir* 7 (1991) 1837–1840.